ENGINEERING

Triboelectric wetting for continuous droplet transport

Wanghuai Xu[1,2]†, Yuankai Jin[1]†, Wanbo Li[1], Yuxin Song[1], Shouwei Gao[1], Baoping Zhang[1], Lili Wang[1], Miaomiao Cui[1], Xiantong Yan[1], Zuankai Wang[1,2]*

Manipulating liquid is of great significance in fields from life sciences to industrial applications. Owing to its advantages in manipulating liquids with high precision and flexibility, electrowetting on dielectric (EWOD) has been widely used in various applications. Despite this, its efficient operation generally needs electrode arrays and sophisticated circuit control. Here, we develop a largely unexplored triboelectric wetting (TEW) phenomenon that can directly exploit the triboelectric charges to achieve the programmed and precise water droplet control. This key feature lies in the rational design of a chemical molecular layer that can generate and store triboelectric charges through agile triboelectrification. The TEW eliminates the requirement of the electric circuit design and additional source input and allows for manipulating liquids of various compositions, volumes, and arrays on various substrates in a controllable manner. This previously unexplored wetting mechanism and control strategy will find diverse applications ranging from controllable chemical reactions to surface defogging.

INTRODUCTION

Developing new techniques that can transport and program liquid with high precision and high adaptivity in a wide range of operating environments is essential to various biomedical (*1*, *2*), optical (*3*, *4*), thermal (*5*–*7*), and electronic applications (*8*). Among various approaches, electrowetting on dielectric (EWOD) or digital microfluidics (*9*–*15*) have revolutionized chemical/biological assays and continue to gain attention owing to many inherent advantages, including high spatial-temporal precision and high level of maneuverability. Recently, new applications, including water harvesting (*16*, *17*), heat transfer (*18*–*20*), and energy harvesting (*21*, *22*), have emerged. Despite its versatility and diversity, the fundamental mechanism lies in tailoring solid-liquid interfacial energy by programming underlying electrodes to induce droplet motion.

Despite extensive progress, the current EWOD technique is susceptible to several limitations. First, effectively modifying the solid-liquid interfacial energy for droplet motion necessitates both size matching and spatial alignment between droplets and underlying electrodes. Thus, a fixed electrode is only suitable for a limited range of droplet sizes, which is challenging for applications involving random droplet distribution. Second, a high level of sophistication in achieving the synchronization between the electric circuit control and droplet response is demanded (*23*). Last, achieving preferential droplet transport also requires the elegant control of interfacial materials with special roughness, wettability, shape, and component, which increases its barrier to integration with the electrical system. Moreover, the seamless integration of the mechanical and electrical components is also susceptible to short circuits during external vibration or misoperation (*24*). All these challenges become more daunting when considering the penetration of the Internet of Things in our daily life, which involves the use of portable devices, especially in energy-limited settings where electricity is not available.
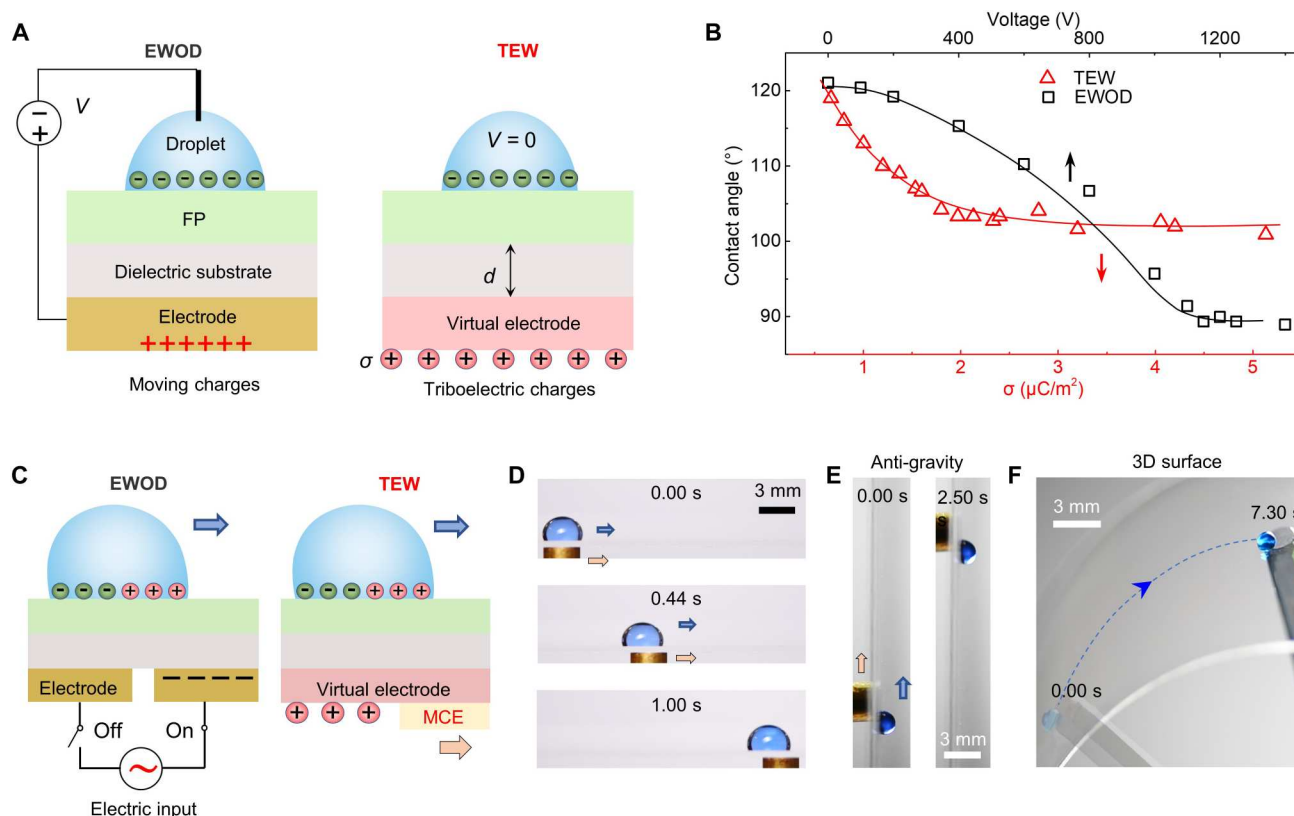
Here, we report a largely unexplored triboelectric wetting (TEW) effect that offers a high level of flexibility and adaptivity for droplet manipulation in a wide range of working conditions without the use of additional electric sources and complicated electrode designs. Different from EWOD, the key innovation of TEW lies in rationally designing a molecular layer that is capable of generating and storing triboelectric charges in response to mechanical triboelectrification (*25*–*28*), thereby generating a driving force on the aimed droplet. Furthermore, this TEW allows for transporting a wide range of liquids (surface tension from 24.3 to 78.3 mN m^{-1}, multiple size scale from 10^{-7} to 10^{-2} m, pH from 1.0 to 11.0, composite from inorganic to organic salt solution, and salt concentration from 10^{-7} to 1.0 M) in various fashions, including three-dimensional (3D) pathway, antigravity, high throughput (six droplets or more), high velocity (151.7 mm s^{-1} or faster), unlimited distance, agile direction steering, and precise droplet anchoring. The TEW is also applicable to flexible substrates and closed microchannels and even adaptive to dynamic environments involving phase transition where fogging or condensate droplets on surfaces can be shed away in an on-demand manner without resorting to special wettability, structural design, and electrical control.

RESULTS

To achieve the TEW effect, we deposited a *N*-(2-aminoethyl)-3-aminopropyltrimethoxysilane (APTS) molecular layer and a hydrophobic fluoropolymer (FP) layer onto the two sides of a thin dielectric layer (500-μm-thick glass slide) using a simple drop-casting method, respectively (Fig. 1A and Materials and Methods). The APTS layer tends to acquire and store abundant positive charges through the contact electrification effect as proposed in our previous work (table S1) (*25*) and thus serves as a "virtual electrode" when in analog to the behavior of the metallic electrode in the EWOD. This electrostatic charge storage ability of virtual electrode, i.e., APTS layer, is beneficial from the electron-donating nature of its amino groups (-NH$_2$) (*29*, *30*), whose presence can be evidenced by the x-ray photoelectron spectroscopy (XPS) spectra and Fourier transform infrared spectroscopy spectra of the APTS-coated surface

[1]Department of Mechanical Engineering, City University of Hong Kong, Hong Kong 999077, China. [2]Department of Mechanical Engineering, The Hong Kong Polytechnic University, Hong Kong 999077, China.
*Corresponding author. Email: zk.wang@polyu.edu.hk
†These authors contributed equally to this work.

Fig. 1. TEW and droplet transport. (**A**) Typical configurations of EWOD and TEW. In the TEW, the substrate consists of a hydrophobic surface (in green, FP), dielectric layer (in gray, thickness d), and virtual electrode (in red, APTS, surface charge density σ). (**B**) Variation of water contact angle as a function of surface charge density σ stored on the virtual electrode in the TEW (red triangle) and the applied voltage in EWOD (black square). The thickness of glass slides is 500 μm. (**C**) Schematic comparison of droplet actuation using EWOD and TEW. Programming the droplet transport in the TEW simply necessitates the sliding of a conductive object on the virtual electrode under the droplet. (**D**) Sequential images showing the continuous transport of a droplet (15 μl) at a constant velocity of 16.7 mm s⁻¹ using an MCE made of a copper rod with a base diameter of 3 mm. (**E**) Sequential images showing the continuous transport of a droplet (4 μl) on a vertical substrate using the MCE. (**F**) Image showing the continuous transport of a droplet (4 μl) on a flexible 3D substrate using the MCE.

(fig. S1). In addition, we chose the FP layer, an interfacial material with hydrophobic and smoothly dense surface with a typical surface roughness of 1.1 nm (fig. S2), to contact the top liquid droplet. The lateral adhesion force F_d of the droplet on the FP surface can be calculated on the basis of the measured advancing angle θ_a and receding angle θ_r, expressed as (*31*, *32*)

$$F_d = kw\gamma(\cos\theta_r - \cos\theta_a)$$

where k, w, and γ are the shape correction coefficient, the contact width, and the liquid-air surface tension of the droplet, respectively. The FP surface enables low-resistance motion for liquids with surface tensions ranging from 21.8 mN m⁻¹ (ethanol) to 72.8 mN m⁻¹ (water) (fig. S3). Moreover, the adhesion strength of FP on the glass substrate can reach 445.6 kPa, which can even withstand the continuous water flush for 10 min without the apparent variation in its hydrophobicity (fig. S4). Notably, the FP layer is transparent and flexible with an elastic modulus of 5 GPa, thereby being applicable to flat, transparent glass slides as well as flexible substrates such as polymer film (fig. S5).

Figure 1A shows the whole configuration of our TEW, consisting of a grounded droplet atop the FP surface and a virtual electrode that is positively charged. Increasing the surface charge density σ

on the entire virtual electrode (2.5 cm × 6 cm) from 0 to 3 μC m⁻² through the tribocharging with other objects leads to the contact angle of a water droplet (5 μl) on the center of FP surface decreasing from 121° to 100° (Fig. 1B), reminiscent of an electrowetting effect in EWOD. Programming the droplet transport simply necessitates the contact and sliding of a conductive object, referred to as mechano-electrode (MCE) (Fig. 1C), on the virtual electrode.

A first glimpse of some key features of the TEW is experimentally shown in Fig. 1D. The contact and sliding of MCE triboelectrify the virtual electrode, providing the driving force to actuate the top droplet. Therefore, without any electric input and circuit design, a droplet on the FP surface can be faithfully guided by a copper MCE moving at a constant velocity (Fig. 1D, fig. S6, and movie S1). Such a new droplet actuation approach persists even on a vertically placed substrate or a 3D curved substrate made of a flexible material [for instance, polyvinyl chloride (PVC)] (Fig. 1, E and F, and movie S2), suggesting its stability and generality. In contrast, in the control sample without a virtual electrode (APTS coating), the droplet cannot be transported under the same actuation of MCE (fig. S7A). In addition to the droplet moving, TEW can also achieve other functions of microfluidic, such as droplet dispensing or splitting (fig. S7B and movie S2). Together, TEW demonstrates superior

droplet control while eliminating the use of external electric inputs and electrode patterns.

To probe the basic mechanisms underlying TEW, we further examine the transient transport behavior of droplet, the generation of triboelectric charges on the underlying virtual electrode, and the potential difference between the virtual electrode and MCE in response to a moving MCE. Initially, the droplet of 6.5 μl remains pinned despite the actuation of a moving copper MCE of 3 mm in diameter at a constant velocity of 16.7 mm s^{-1} (fig. S8). With time progress, the droplet gradually transforms into a longer and narrower drop shape, with the advancing contact angle θ_{EA} decreasing from 121° to 104.8° and the receding contact angle θ_{ER} reducing from 121° to 107.8° (Fig. 2A). After reaching such a critical contact angle at $t = 0.12$ s, the droplet transits to the kinetic stage and maintains a synchronous motion with the MCE with a relatively stable contact angle of around 108°. Throughout the two stages, we measured the continuous generation of positive triboelectric charges $Q_V(t)$ on the virtual electrode at a rate of 0.12 nC mm^{-1} (Fig. 2B and Materials and Methods) and an electrostatic potential difference $V_{V\text{-}M}$ between the virtual electrode and MCE is built

accordingly. As shown in Fig. 2C, the peak $V_{V\text{-}M}$ reaches 773.7 V for an MCE displacement L of 2 mm.

The newly built electrostatic voltage as a result of continuous triboelectrification between the virtual electrode and MCE is analogous to the voltage across the EWOD electrodes, which gives rise to an imposed electrostatic field or electric surface stress vector $\boldsymbol{T_e}$ acting on the droplet (fig. S9), which can be calculated by the dot product of the Maxwell stress tension $T_{e,ij}$ and the surface unit normal vector $\mathbf{n}$

$$\boldsymbol{T_e} = [T_{e,ij}] \bullet \mathbf{n} \text{ with } T_{e,ij} = \varepsilon_0(E_i E_j - \frac{\delta_{ij}}{2}E^2), i,j = x,y,z$$

where ε_0, δ_{ij}, and E are the permittivity of air, Kronecker delta function, and the magnitude of the electric field intensity, respectively. We calculated the distribution of $\boldsymbol{T_e}$ on the droplet through a finite element analysis using COMSOL Multiphysics (version 5.4). With the actuation of the MCE, the interfacial downward $\boldsymbol{T_e}$ at the water/FP contact line increases (fig. S10), leading to the wetting effect of the droplet as shown in Fig. 2A. Meanwhile, the lateral component of the $\boldsymbol{T_e}$, $T_{e,x}$, on the convex top surface centralizes on the front
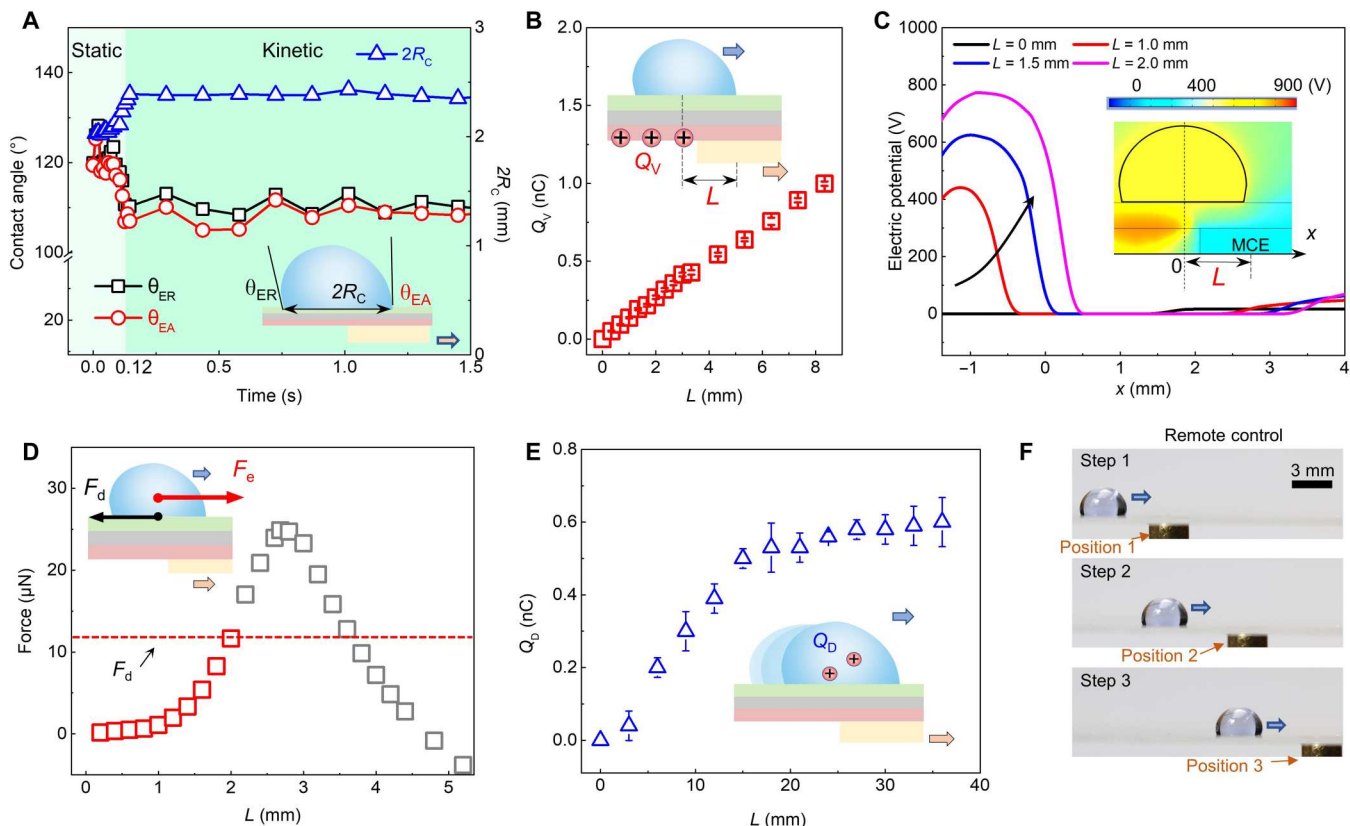
Fig. 2. Actuation mechanism. (**A**) Time scale evolution of the water contact angle (θ_{EA} and θ_{ER}) and the lateral base diameter ($2R_C$) in response to the actuation of the MCE. (**B**) Charge generation (Q_V) on the virtual electrode owing to the triboelectrification with the MCE as a function of sliding displacement L of the MCE. Data are means ± SEM with three independent measurements. (**C**) Numerically calculated potential distribution (V) contour along with the centerline of the sliding path on the virtual electrode ($y = 0$, $z = -0.5$ mm) with various L of MCE (presented as the lines with various colors). The electrostatic potential of the MCE is set at 0 V. Inset shows the potential distribution ($y = 0$) when $L = 2$ mm. (**D**) Driving force that was numerically calculated as a function of L through the surface integral of $T_{e,x}$ over the droplet (6.5 μl). When $L = 2$ mm, the driving force increases to be larger than the lateral adhesion force acting on the droplet, where the red and gray symbols represent the situations before and after the droplet actuation. (**E**) Charge generation in the droplet (6.5 μl) as a function of droplet displacement during actuation. The measured droplet charge increases and saturates at around 0.60 nC. Data are means ± SEM with three independent measurements. (**F**) Sequential images showing the three-step successive remote droplet transport. This precise, remote control and long-distance transportation can be achieved by changing the position of the MCE.

surface and rear surface of the droplet, with a larger value on the front surface (fig. S11). The integration of the numerically calculated $T_{e,x}$ over the droplet surface yields the driving force F_e acting on the droplet, $F_e = \oint T_{e,x} dS$. As shown in Fig. 2D, when the MCE moves to $L = 2$ mm, F_e increases to 12.6 μN, large enough to overcome the adhesion force F_d exerting on the droplet (fig. S3), which is consistent with the droplet dynamic in our experiments. Notably, the motion of droplet enables to further obtain additional positive triboelectric charges through the contact electrification with the FP surface (Fig. 2E) (*33*), increasing the electrostatic interaction, as reflected by the high-velocity (~151.7 mm s^{-1}) and remote droplet transport (Fig. 2F, fig. S12, and movie S3). The working mechanisms underlying the TEW are different from those methods based on surface charge printing (*34*) or electrostatic induction (*35*). In the former, a prestored charge gradient on superhydrophobic surfaces is needed to provide the driving force for droplet motion, whereas in the latter both high electrical conductivity of substrate and high-voltage power source are required to induce coulomb attraction for droplet motion.

The manifestation of TEW-induced droplet transport demands the elegant regulation of the surface charge density σ on the virtual electrode and substrate thickness d. Note that σ can be easily modulated by tailoring the concentrations of APTS during fabrication steps (fig. S13). The magnitude of electrostatic force F_e derived from the simulation on various substrates is sensitive to charge density σ and substrate thickness d (fig. S14). As shown in Fig. 3A, either increasing σ or decreasing d facilitates effective droplet transport, in which the critical σ and d for successfully actuating the droplet are in good agreement with our simulation results. Moreover, even after 500 MCE sliding cycles, the charge generation on the virtual electrode still sustains, which is beneficial for long-term droplet manipulation (Fig. 3B). Note that the charge generation is affected by the surrounding temperature and humidity (fig. S15).

The TEW effect also manifests when the virtual electrode and MCE are made of other materials that can generate sufficient electrostatic charges but with opposite polarity. As shown in Fig. 3C, we selected a 50-μm-thick commercial Nylon film to attach on one side of a glass substrate to serve as a virtual electrode and a commercial fluorinated ethylene propylene (FEP) rod to serve as an MCE. The triboelectrification between the nylon and FEP can generate a surface charge density of 34 μC m^{-2} comparable to that between APTS and copper (40 μC m^{-2}), which is sufficient for continuous droplet transport (fig. S16). The TEW effect enables manipulation of multidroplet arrays, droplets with volumes ranging from tens of nanoliters to several microliters (fig. S17 and movie S4), and liquids of different surface tensions, viscosities, conductivities, compositions, and dielectric constants (Fig. 3D and fig. S18). The TEW demonstrates overwhelmingly collective performances over counterparts relying on EWOD or triboelectric charges (*34–38*) in the aspects of manipulating condition, control precision, and versatility for the substrate materials (Fig. 3E).

DISCUSSION
Eliminating the need of complicated electrodes and power sources in TEW imparts broad application scenarios, especially in source-limited settings (movie S5). The droplets with reduced volume can serve as tiny reactors for low-dose chemical reactions such as the

chromogenic reaction between a phenolphthalein reagent droplet, an aqueous alkaline droplet (pH = 12) and an aqueous acid droplet (pH = 2) (Fig. 4A). In addition, droplets can also be transported to carry cargo, such as bovine serum albumin (BSA) solution (Fig. 4B), which otherwise can be readily adsorbed on hydrophobic surfaces (*39*). The flexibility associated with the manipulation approach also enables the droplet sorting without a preset pathway (Fig. 4C). Figure 4D shows that an ethanol plug can be guided to dissolve and remove a ferric chloride (FeCl₃) particle in a closed capillary by using a conductive sleeve-like aluminum MCE wrapping around the capillary. Such a process in a confined environment is fully visualized due to the high-transmission coatings, which is of importance for tracking real-time reactions.

Another intriguing feature of TEW is its ability to collectively shed randomly distributed multi-sized droplet clusters from surfaces even in complex operating environments involving phase transition. Droplet formation and accretion on underlying solid surface (*40, 41*) as a result of adsorption and condensation are widely manifested in many industrial processes, which reduce optical transmittance (*42*), delay heat transfer, and accelerate icing (*43*). As shown in Fig. 4E, we demonstrate that numerous fog droplets on the surface could be transported by a moving MCE, then coalesce with other droplets in their pathway, and finally be swept away from the surface by the electrostatic force and gravity force. After a four-time reciprocating motion of MCE, the droplet area fraction on the surface is reduced by 96%, preserving a signature of an active antifogging strategy capable of dynamically shedding away droplets in an on-demand manner, while the control samples without the construction of virtual electrode show no apparent reduction in the fog-covering area (Fig. 4F and fig. S19). Together, efficient fog removing can be obtained in an on-demand manner without resorting to special wettability, structural design, and electric circuit control.

In summary, we report a largely unexplored TEW effect that can directly exploit the triboelectric charges to achieve programmable and precise water droplet control. The TEW effect enables transporting and manipulating the liquid of various compositions, volumes, and arrays in a high-speed and controllable manner. Together with its generality over a wide range of shapes and materials of the substrate, the TEW effect will find diverse applications ranging from controllable chemical reactions to fluid engineering where droplet manipulation is required, especially in electric source-limited settings.

MATERIALS AND METHODS
Materials
Amorphous fluoroplastics precursor (6%; Chemours, Teflon AF 1601), amorphous FP CYTOP (AGC Chemicals, CTL-809M), fluorinated solvent solution (AGC Chemicals, SOLV180), APTS (95%; Dieckmann), deionized water [resistivity of 18.3 megohm·cm, produced by a deionized water system (DINEC, Hong Kong)], hydrogen peroxide solution (30%; Sigma-Aldrich), sulfuric acid solution (≥99%; Sigma-Aldrich), BSA (≥99%; Sigma-Aldrich), tris hydrochloride buffer (>99%; Sigma-Aldrich), sodium hydroxide (≥98%; Sigma-Aldrich), hydrochloric acid (37% in water), ferric chloride (≥99%; Sigma-Aldrich), ethanol (≥99%; Sigma-Aldrich), glycerin (≥99%; Sigma-Aldrich), glycol (≥99%; Sigma-Aldrich), sodium chloride (≥99%; Sigma-Aldrich), and sodium alga acid (low-
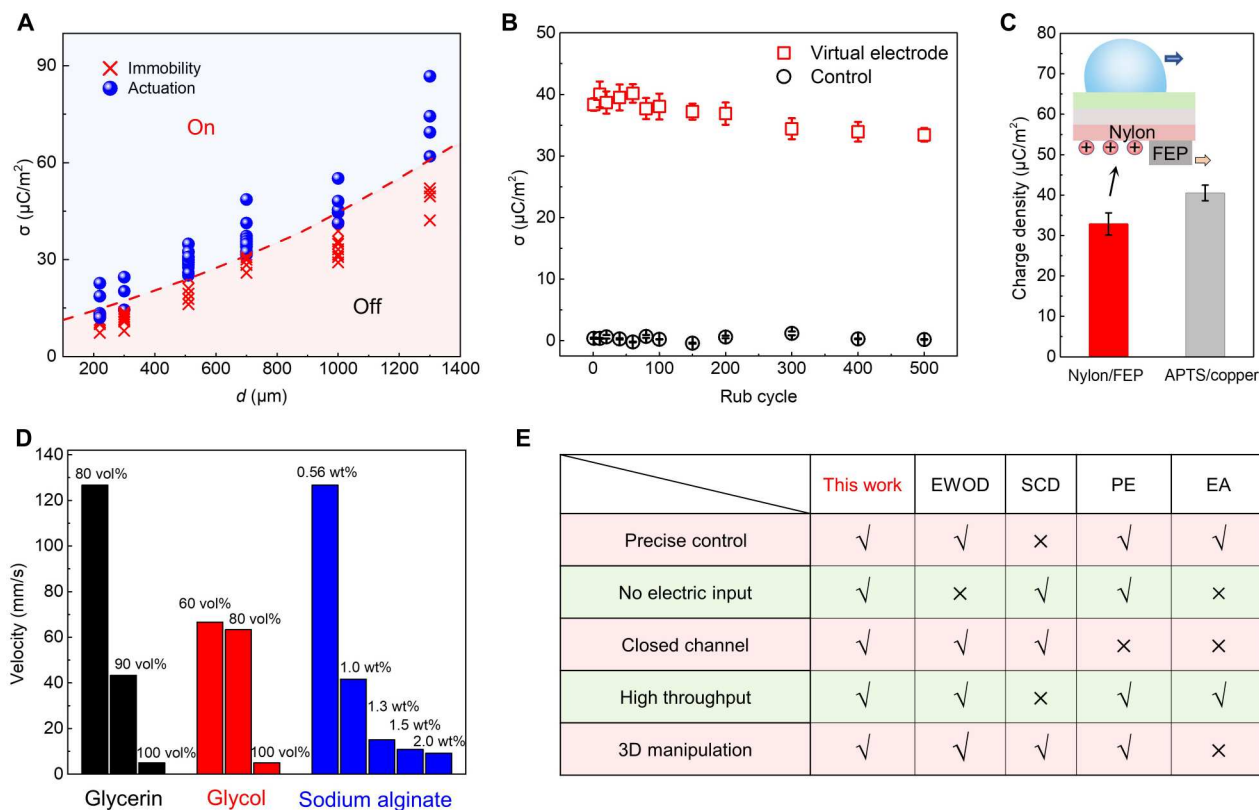
Fig. 3. Generality of TEW-mediated droplet transport. (**A**) Effects of surface charge density σ on virtual electrode and thickness d of the glass substrate on droplet actuation. Blue or "on" region (symbols and background) denotes that the droplets were actuated. Red or "off" region (symbols and background) denotes that the droplets remained pinned. Each dot represents a test. Dashed line (in red) denotes the numerically simulated critical σ and d for the successful actuation of the droplet. The droplet size is 6.5 µl. (**B**) Durability test of the virtual electrode. After over 500 times droplet transport cycle, the triboelectric charge density generated on the virtual electrode drops slightly from 40 to 36.9 µC m⁻² while keeping around zero on the control surface without the construction of virtual electrode. Data are means ± SEM with three independent measurements. (**C**) Comparison of charge generation from the triboelectrification between nylon and fluorinated ethylene propylene (FEP) and between APTS and copper. Inset shows the schematic of droplet actuation using TEW effect based on the triboelectrification between the nylon and FEP. (**D**) Maximum transport velocity of various liquids (glycerin, glycol, and sodium alginate) with various concentrations. (**E**) Comparison between the TEW and previously reported charge-based droplet transports, including EWOD, surface charge density gradient (34) (SCD), electrostatic attraction (EA) (35), and photopyroelectric (PE) from five items. "√" and "×" denote yes and no, respectively.

viscosity model; Sigma-Aldrich) were used without further purification. Ultra-Ever Dry was purchased from Ultra Tech International Inc. Copper was purchased from the common hardware stores in Hong Kong.

Substrate preparation
To achieve TEW, we constructed the virtual electrode and the hydrophobic FP layer onto the two sides of a thin glass slide using a simple drop-casting method, respectively. The glass slide was first cleaned in piranha solution (hydrogen peroxide solution:sulfuric acid = 3:1) for 30 min. To construct the virtual electrode, one side of the glass slide was fully covered with an ethanol solution of APTS (0.023 M) for 20 min, then wiped with air-laid papers, and heated to remove all ethanol. To construct the FP surface, the other side of the glass slide was drop-casted with the FP solution consisting of Teflon AF and CYTOP (volume ratio, V_Teflon AF:V_CYTOP:V_SOLV180 = 1:1:4) and heated at 180°C for 20 min to remove all solvent. Upon curing at 180°C, the FP solution was transformed into a smooth and dense FP film (fig. S2). Note that the APTS-modified surface can be easily charged by contacting or rubbing against other objects, such as air-

laid papers, and the charge density can be easily modulated by rubbing it against the different materials. The flexible substrate with the PVC film serving as the substrate was fabricated using the same method as that based on the glass slide. To achieve TEW in a closed microchannel, a 3-mm-thick glass capillary was first covered by the FP solution in the inner surface, followed by being heated to form a solid film of FP layer. Then, the virtual electrode on the outer surface of the capillary was constructed using the same method as that in the case of the flat glass slide.

Droplet manipulation
In a typical process, liquid droplets were first placed lightly onto the upward surface (FP surface) of the substrate that was suspended in mid-air. An MCE made of a copper rod (3 mm in base diameter) was then lightly contacted with the virtual electrode (APTS surface). Then, the MCE was controlled by either a hand or a linear stage consisting of a custom-made step motor to actuate the droplet. The detailed droplet behavior in response to the actuation of the MCE was monitored by a high-speed camera (Photron FASTCAM SA4) at a typical recording speed of 6000 frames per
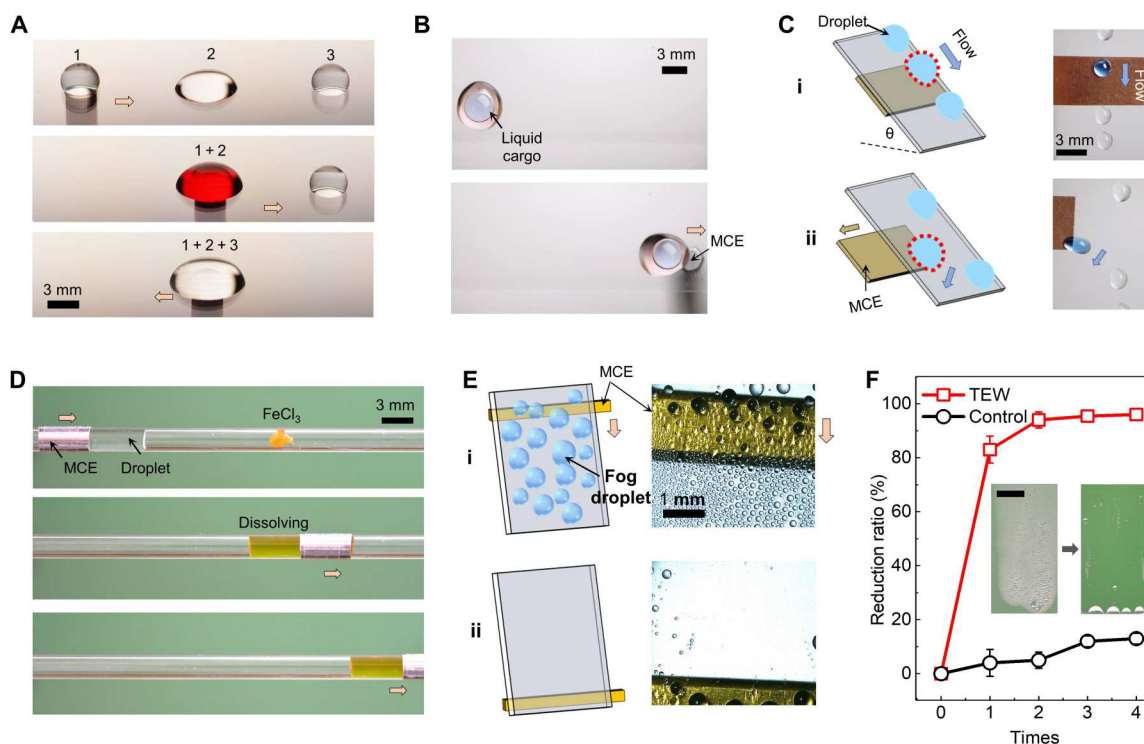
Fig. 4. Applications of TEW. (**A**) Sequential images shows droplets serve as reactors and can be transported for chemical reaction, including color reaction (1 to 2) and neutralization reaction (3 to 2), where droplets labeled 1, 2, and 3 denote sodium hydroxide, phenolphthalein reagent, and hydrochloric acid, respectively. (**B**) Sequential images showing the continuous transport of a liquid cargo, i.e., a BSA solution droplet (10 μg ml^{-1}; in blue) of 20 μl, which is carried by a cetane droplet (in pink). (**C**) Schematic drawings (i and ii) showing the droplet sorting using TEW (left). We continuously generated droplets onto the substrate placed at an angle of 30° from the horizon plane to form an array of droplets, some of which are dyed for being sorted. Under the mechanical actuation of the MCE, the dyed droplet sliding along the surface changes its original path and removes from the other droplets in the droplet array, i.e., be sorted (right). (**D**) Sequential images showing the dissolving and removing of a ferric chloride particle using the closed-microchannel TEW. (**E**) Schematic drawings (i and ii) showing TEW for surface defogging (left). Sequential images showing fog removing using a slender MCE (right). (**F**) Comparison of the fog area loss between the TEW and on the control surface without the construction of virtual electrode. Scale bar, 1 cm. Data are means ± SEM with three independent measurements.

second. The relative humidity was kept constant at approximately 60%, and the room temperature was 26°C.

Surface characterization

The transmission of light with wavelengths ranging from 400 to 1100 nm was measured with an ultraviolet-visible spectrometer (PerkinElmer Lambda 35). The surface element component of the virtual electrode was analyzed by XPS (ESCALAB 250Xi multifunctional spectrometer, Thermo Fisher Scientific). The static and dynamic contact angles of water on all samples were measured by a Krüss DSA100 contact angle goniometer at room temperature of 26°C with a ~60% relative humidity.

Charge measurement

To measure the charge generation on the virtual electrode, we inserted the charged substrate into a Faraday cup connected to a nanocoulomb meter (the other terminal was grounded) and then read the display. To measure the charge generation on the virtual electrode during the droplet manipulation, the conductive MCE was connected to the measured terminal of the nanocoulomb meter (the reference terminal was grounded) using the method shown in fig. S20A. After being charged by the MCE, the charge generated on the virtual electrode equals the charge flowing

through the nanocoulomb meter when the separation distance between the virtual electrode and MCE is enough (about 10 cm). To measure the charge generation in the droplet, we connected the droplet with the measure terminal of the nanocoulomb meter, whereas the reference terminal was connected to the MCE shown in fig. S20B.

Numerical study of the droplet transient in response to the MCE actuation

We conducted the numerical study, including the simulation of the potential distribution, electric field distribution, corresponding electric stress tensor distribution, and the net driving force calculation, by using a finite element method (COMSOL Multiphysics). In the absence of body force and electric body charge, the governing equations are expressed as follows

$$\boldsymbol{E} = -\nabla \bullet V$$

$$\nabla \bullet \boldsymbol{D} = 0$$

where $\boldsymbol{E}$ is the strength of the electric field, V is the electric potential, and $\boldsymbol{D}$ is the electric displacement, respectively. Charge density boundary conditions were given by the measured values, whereas

the potential of the MCE was set as zero. The droplet deformation was small and therefore negligible in our simulations.

Given the fixed droplet position, we calculated the driving force on the droplet by varying the position of the MCE to simulate the MCE motion. For a droplet of 6.5 μl, the calculated driving force first increases and then decreases, showing a maximum value of 24.9 μN when the MCE is tangent to the droplet. The competition between the maximum driving force determines if the droplet can be effectively actuated.

Supplementary Materials

This PDF file includes:
Supplementary Discussions
Figs. S1 to S24
Table S1

Other Supplementary Material for this manuscript includes the following:
Movies S1 to S5

REFERENCES AND NOTES

1. W. Li, L. Zhang, X. Ge, B. Xu, W. Zhang, L. Qu, C.-H. Choi, J. Xu, A. Zhang, H. Lee, D. A. Weitz, Microfluidic fabrication of microparticles for biomedical applications. *Chem. Soc. Rev.* **47**, 5646–5683 (2018).

2. S.-Y. Teh, R. Lin, L.-H. Hung, A. P. Lee, Droplet microfluidics. *Lab Chip* **8**, 198–220 (2008).

3. C. Hao, Y. Liu, X. Chen, Y. He, Q. Li, K. Y. Li, Z. Wang, Electrowetting on liquid-infused film (EWOLF): Complete reversibility and controlled droplet oscillation suppression for fast optical imaging. *Sci. Rep.* **4**, 6846 (2014).

4. S. Kuiper, B. Hendriks, Variable-focus liquid lens for miniature cameras. *Appl. Phys. Lett.* **85**, 1128–1130 (2004).

5. D. Baratian, R. Dey, H. Hoek, D. van den Ende, F. Mugele, Breath figures under electrowetting: Electrically controlled evolution of drop condensation patterns. *Phys. Rev. Lett.* **120**, 214502 (2018).

6. M. Jiang, Y. Wang, F. Liu, H. Du, Y. Li, H. Zhang, S. To, S. Wang, C. Pan, J. Yu, D. Quéré, Z. Wang, Inhibiting the Leidenfrost effect above 1,000° C for sustained thermal cooling. *Nature* **601**, 568–572 (2022).

7. N. Li, L. Wu, C. Yu, H. Dai, T. Wang, Z. Dong, L. Jiang, Ballistic jumping drops on superhydrophobic surfaces via electrostatic manipulation. *Adv. Mater.* **30**, 1703838 (2018).

8. R. A. Hayes, B. J. Feenstra, Video-speed electronic paper based on electrowetting. *Nature* **425**, 383–385 (2003).

9. W. C. Nelson, C.-J. C. Kim, Droplet actuation by electrowetting-on-dielectric (EWOD): A review. *J. Adhes. Sci. Technol.* **26**, 1747–1771 (2012).

10. F. Mugele, J.-C. Baret, Electrowetting: From basics to applications. *J. Phys. Condens. Matter* **17**, R705–R774 (2005).

11. S. K. Cho, H. Moon, C.-J. Kim, Creating, transporting, cutting, and merging liquid droplets by electrowetting-based actuation for digital microfluidic circuits. *J. Microelectromech. Syst.* **12**, 70–80 (2003).

12. G. McHale, C. V. Brown, M. I. Newton, G. G. Wells, N. Sampara, Dielectrowetting driven spreading of droplets. *Phys. Rev. Lett.* **107**, 186101 (2011).

13. J. Li, N. S. Ha, T. ʻ. Lʻ. Liu, R. M. van Dam, C. J. ʻCJʼ Kim, Ionic-surfactant-mediated electro-dewetting for digital microfluidics. *Nature* **572**, 507–510 (2019).

14. Y. Liu, J. Wei, E. Chen, L. Qin, Y. Yu, Photocontrol of fluid slugs in liquid crystal polymer microactuators. *Nature* **537**, 179–184 (2016).

15. E. Bormashenko, R. Pogreb, Y. Bormashenko, R. Grynyov, O. Gendelman, Low voltage reversible electrowetting exploiting lubricated polymer honeycomb substrates. *Appl. Phys. Lett.* **104**, 171601 (2014).

16. R. Yan, T. S. McClure, I. H. Jasim, A. K. R. Koppula, S. Wang, M. Almasri, C. L. Chen, Enhanced water capture induced with electrowetting-on-dielectric (EWOD) approach. *Appl. Phys. Lett.* **113**, 204101 (2018).

17. S. Högnadóttir, K. Kristinsson, H. G. Thormar, K. Leosson, Increased droplet coalescence using electrowetting on dielectric (EWOD). *Appl. Phys. Lett.* **116**, 073702 (2020).

18. A. Sur, Y. Lu, C. Pascente, P. Ruchhoeft, D. Liu, Pool boiling heat transfer enhancement with electrowetting. *Int. J. Heat Mass Transf.* **120**, 202–217 (2018).

19. R. S. Hale, V. Bahadur, Electrowetting-based microfluidic operations on rapid-manufactured devices for heat pipe applications. *J. Micromech. Microeng.* **27**, 075004 (2017).

20. H. J. Cho, J. P. Mizerak, E. N. Wang, Turning bubbles on and off during boiling using charged surfactants. *Nat. Commun.* **6**, 1–7 (2015).

21. J. K. Moon, J. Jeong, D. Lee, H. K. Pak, Electrical power generation by mechanically modulating electrical double layers. *Nat. Commun.* **4**, 1–6 (2013).

22. T. Krupenkin, J. A. Taylor, Reverse electrowetting as a new approach to high-power energy harvesting. *Nat. Commun.* **2**, 1–8 (2011).

23. H. Song, R. F. Ismagilov, Millisecond kinetics on a microfluidic chip using nanoliters of reagents. *J. Am. Chem. Soc.* **125**, 14613–14619 (2003).

24. H. Liu, S. Dharmatilleke, D. K. Maurya, A. A. O. Tay, Dielectric materials for electrowetting-on-dielectric actuation. *Microsyst. Technol.* **16**, 449–460 (2009).

25. Y. Jin, W. Xu, H. Zhang, H. Zheng, Y. Cheng, X. Yan, S. Gao, D. Wang, Y. Zi, F. Zhou, Z. Wang, Complete prevention of contact electrification by molecular engineering. *Matter* **4**, 290–301 (2021).

26. D. J. Lacks, T. Shinbrot, Long-standing and unresolved issues in triboelectric charging. *Nat. Rev. Chem.* **3**, 465–476 (2019).

27. A. Z. Stetten, D. S. Golovko, S. A. L. Weber, H. J. Butt, Slide electrification: Charging of surfaces by moving water drops. *Soft Matter* **15**, 8667–8679 (2019).

28. Z. L. Wang, A. C. Wang, On the origin of contact-electrification. *Mater. Today* **30**, 34–51 (2019).

29. S.-H. Shin, Y. H. Kwon, Y. H. Kim, J. Y. Jung, M. H. Lee, J. Nah, Triboelectric charging sequence induced by surface functionalization as a method to fabricate high performance triboelectric generators. *ACS Nano* **9**, 4621–4627 (2015).

30. S. Lin, M. Zheng, J. Luo, Z. L. Wang, Effects of surface functional groups on electron transfer at liquid-solid interfacial contact electrification. *ACS Nano* **14**, 10733–10741 (2020).

31. D. Daniel, J. V. I. Timonen, R. Li, S. J. Velling, J. Aizenberg, Oleoplaning droplets on lubricated surfaces. *Nat. Phys.* **13**, 1020–1025 (2017).

32. N. Gao, F. Geyer, D. Pilat, S. Wooh, D. Vollmer, H.-J. Butt, R. Berger, How drops start sliding over solid surfaces. *Nat. Phys.* **14**, 191–196 (2017).

33. X. Li, P. Bista, A. Z. Stetten, H. Bonart, M. T. Schür, S. Hardt, F. Bodziony, H. Marschall, A. Saal, X. Deng, R. Berger, S. A. L. Weber, H.-J. Butt, Spontaneous charging affects the motion of sliding drops. *Nat. Phys.* **18**, 713–719 (2022).

34. Q. Sun, D. Wang, Y. Li, J. Zhang, S. Ye, J. Cui, L. Chen, Z. Wang, H. J. Butt, D. Vollmer, X. Deng, Surface charge printing for programmed droplet transport. *Nat. Mater.* **18**, 936–941 (2019).

35. Y. Jin, W. Xu, H. Zhang, R. Li, J. Sun, S. Yang, M. Liu, H. Mao, Z. Wang, Electrostatic tweezer for droplet manipulation. *Proc. Natl. Acad. Sci. U.S.A.* **119**, e2105459119 (2022).

36. X. Tang, W. Li, L. Wang, Furcated droplet motility on crystalline surfaces. *Nat. Nanotechnol.* **16**, 1106–1112 (2021).

37. H. Dai, C. Gao, J. Sun, C. Li, N. Li, L. Wu, Z. Dong, L. Jiang, Controllable high-speed electrostatic manipulation of water droplets on a superhydrophobic surface. *Adv. Mater.* **31**, e1905449 (2019).

38. J. Nie, Z. Ren, J. Shao, C. Deng, L. Xu, X. Chen, M. Li, Z. L. Wang, Self-powered microfluidic transport system based on triboelectric nanogenerator and electrowetting technique. *ACS Nano* **12**, 1491–1499 (2018).

39. A. R. Wheeler, H. Moon, C. A. Bird, R. R. Ogorzalek Loo, C. J. ". C. J.". Kim, J. A. Loo, R. L. Garrell, Digital microfluidics with in-line sample purification for proteomics analyses with MALDI-MS. *Anal. Chem.* **77**, 534–540 (2005).

40. T. Mouterde, G. Lehoucq, S. Xavier, A. Checco, C. T. Black, A. Rahman, T. Midavaine, C. Clanet, D. Quéré, Antifogging abilities of model nanotextures. *Nat. Mater.* **16**, 658–663 (2017).

41. R. Dey, J. Gilbers, D. Baratian, H. Hoek, D. van den Ende, F. Mugele, Controlling shedding characteristics of condensate drops using electrowetting. *Appl. Phys. Lett.* **113**, 243703 (2018).

42. M. C. Al Naboulsi, H. Sizun, F. de Fornel, Fog attenuation prediction for optical and infrared waves. *Opt. Eng.* **43**, 319–329 (2004).

43. D. Attinger, C. Frankiewicz, A. R. Betz, T. M. Schutzius, R. Ganguly, A. Das, C.-J. Kim, C. M. Megaridis, Surface engineering for phase change heat transfer: A review. *MRS Energy Sustain.* **1**, E4 (2014).

Science Advances

Triboelectric wetting for continuous droplet transport

Wanghuai Xu, Yuankai Jin, Wanbo Li, Yuxin Song, Shouwei Gao, Baoping Zhang, Lili Wang, Miaomiao Cui, Xiantong Yan, and Zuankai Wang

View the article online
https://www.science.org/doi/10.1126/sciadv.ade2085
Permissions
https://www.science.org/help/reprints-and-permissions

Use of this article is subject to the Terms of service